Neutral pion masses within a hot and magnetized medium in a lattice-improved soft-wall AdS/QCD model

Nanxiang Wen,[1] Xuanmin Cao,[1,*] Jingyi Chao,[2,†] and Hui Liu[1]

[1]*Department of Physics and Siyuan Laboratory, Jinan University, Guangzhou 510632, China*
[2]*College of Physics and Communication Electronics, Jiangxi Normal University, Nanchang, Jiangxi 330022, China*

(Received 20 February 2024; accepted 25 March 2024; published 22 April 2024)

We investigate chiral phase transitions and the screening masses, pole masses, and thermal widths of neutral pion mesons with finite temperature T and magnetic field B in a lattice-improved AdS/QCD model, which is constructed by fitting the lattice results of the pseudocritical temperatures $T_{\mathrm{pc}}(B)$. Specifically, we find that the chiral condensate σ undergoes a crossover phase transition demonstrating distinct magnetic catalysis and inverse magnetic catalysis effects in very low- and high-temperature regions with fixed finite B, respectively. For the screening masses, we find that the longitudinal component decreases with B at very low and high temperatures and increases with B near T_{pc}. The transverse component always increases with B at fixed T. However, both the longitudinal and transverse screening masses increase with T at fixed B. Furthermore, we find that the pole mass decreases with the increase of B or T. It is interesting to note that the thermal width shows similar behavior to the longitudinal screening masses in the very-high-temperature region.

DOI: 10.1103/PhysRevD.109.086021

I. INTRODUCTION

The properties of strong interactions in the presence of a substantial external magnetic field have been studied extensively in recent years. The reason for this is that, in off-center heavy-ion collisions, strong magnetic fields of about 10^{18} to 10^{19} Gauss, or $|eB| \sim m_\pi^2$ to $15m_\pi^2$, are produced when two fast-moving nuclei collide [1–3]. In the presence of such a strong external magnetic field, not only is the phase diagram of quantum chromodynamics (QCD) matter altered [4–6] but also many novel and interesting phenomena will arise due to the interaction between the magnetic field and the nonperturbative properties of non-Abelian gauge theory, including the chiral magnetic effect [7–10], disputable superconductivity in magnetized vacuum [11,12], neutral pion condensation [13], diamagnetism at low temperature, and paramagnetism at high temperature [14].

It has been shown that in a simplified effective theory, certain properties of the equilibrium plasma can be obtained by a reduction of the dimension from D to $D-1$ at finite temperature. Furthermore, in the strong B limit the longitudinal and transverse spaces are decoupled, allowing us to reduce the transverse dimensions. Compared to magnetized matter at zero temperature, several unexpected phenomena have arisen, showing the interplay between the anisotropies induced by thermal excitation and the magnetic field. The most famous effect is that the chiral order parameter, characterized by spontaneous chiral symmetry breaking (SSB), is catalyzed by the magnetic field in the vacuum, known as magnetic catalysis (MC) in various models, including the two-flavor QCD system [15–17]. However, the chiral pseudocritical temperature T_{pc} decreases with increasing B in QCD matter. This is beyond the prediction of low-energy effective theories or model calculations, known as inverse magnetic catalysis (IMC) [4,18]. In order to solve this puzzle, extensive work has been done using numerous approaches (see recent reviews, e.g., Ref. [19]). Among these explanations and calculations, the proper implementation of thermal modification is particularly important.

Therefore, we pay more attention to the properties of the light mesons at finite temperature. Since the pattern of SSB is $U(1)_{I_3} \otimes U(1)_{AI_3} \to U(1)_{L+R}$, the neutral pion is the only Goldstone boson in two-flavor QCD. It plays a unique role in low-energy hadronic physics [20–24]. Our motivation for the study of thermal effects on π^0 is the observation that reliable information on the temperature modification of magnetized hadronic properties is still lacking. Since the temperature breaks the Lorentz invariance, this implies that one needs not only the pole mass

*Corresponding author: caoxm@jnu.edu.cn
†Corresponding author: chaojingyi@jxnu.edu.cn

m_{pole}, which describes the positions of the poles in the particle's propagators, but also the screening masses m_{scr}, which characterize the exponential decay of static propagators. The relationship between the screening mass and the pole mass is determined by the dispersion relation: $m_{\mathrm{scr}} = m_{\mathrm{pole}}/u$. In addition, there are two types of screening masses because the magnetic field breaks the $O(3)$ rotation symmetries to $O(2)$: $m_{\mathrm{scr},\parallel}$ and $m_{\mathrm{scr},\perp}$ for the masses along the direction of B and those perpendicular to it, respectively. As required by the law of causality, pointed out by Ref. [21], it can be deduced that $u_{\perp,\parallel} < 1$. In addition, since motion along the transverse direction is suppressed compared to motion along the longitudinal direction, a naive estimate is that $u_\perp < u_\parallel$. We conclude that $u_\perp < u_\parallel < 1$, so $m_{\mathrm{scr},\perp} > m_{\mathrm{scr},\parallel} > m_{\mathrm{pole}}$ [21]. Over the decades, numerous models have been developed for studying the vacuum and thermal properties of hadrons with a magnetic field. These frameworks include lattice QCD (LQCD) [23,25–29], chiral perturbation theory (χPT) [30–32], the Nambu–Jona-Lasinio model (NJL) [21,22,33–35], and the functional renormalization group (FRG) [24,36,37].

Besides the traditional methods, the discovery of the famous anti–de Sitter/conformal field theory (AdS/CFT) correspondence [38–40] offers a powerful tool for investigating strong coupling problems of QCD. In the framework of the bottom-up approach, several holographic QCD (HQCD) models have been constructed, e.g., the hard-wall model [41] and soft-wall AdS/QCD model [42] for chiral dynamics and hadronic physics, the Einstein-Maxwell-dilaton system [43–46] for thermodynamics, the light-front holographic QCD model [47] for hadronic physics, and so on.

Among those HQCD models, we take the soft-wall model as the starting point of this work since it can give a good description of hadronic physics [48–58] as well as spontaneous chiral symmetry breaking [59,60]. Furthermore, the mass plane phase diagram from the soft-wall model [61,62] is shown to be qualitatively consistent with the so-called "Columbia plot" [63,64]. Since the model is constructed based on symmetry, it is quite direct to introduce the conserved current. Therefore, it is also convenient to extend the study to many different conditions, such as finite baryon/isospin densities [65–67], rotating mediums [68], and nonequilibrium phase transitions [69]. In addition, the thermal properties as well as the Goldstone nature of pions have been systematically investigated in [70–73].

By introducing the magnetic field in the holographic models, it is possible to study the properties of QCD in the hot magnetized medium [74–77]. In Ref. [74], the authors obtained the IMC effect on chiral condensation and its pseudocritical temperature T_{pc}. Additionally, the results from Ref. [77] showed that chiral condensation not only exhibits an IMC effect near T_{pc} but also demonstrates an MC effect at low temperatures. However, those studies are based on perturbative expansion solutions, and the magnetic field strength cannot be extended to large values. Furthermore, those studies only analyze the order parameter, and the properties about the Goldstone bosons are absent. Therefore, in this work, we will try to solve the full magnetized background and study the thermal pions under this background. Furthermore, the variation of the chiral phase transition temperature T_{pc} with B in soft-wall AdS/QCD models differs from the lattice simulation results [4,18]. Hence, we posit that those soft-wall AdS/QCD models should undergo alterations when introducing the magnetic field. Inspired by the magnetic field-dependent four-fermion coupling constant $G(B)$ introduced in Ref. [22], we will modify the 5D mass of the soft-wall AdS/QCD model by introducing a polynomial $g(B)$, which is considered an effective coupling between the dilaton and the scalar field, or, in some sense, the coupling between the gluonic and chiral sectors. We will fit such an effective coupling by comparing the data of $T_{\mathrm{pc}}(B)$ with the lattice simulation [4]. After fitting the model, we will systematically study the thermal properties of the neutral pions.

This paper is organized into the following sections. In Sec. II, after introducing the Einstein-Maxwell system with the backreaction of the magnetic field, we solve the Einstein-Maxwell equation and obtain the complete numerical background solutions with different temperatures T and magnetic field strength B. In Sec. III, we modify the expression of the 5D mass m_5 in the AdS/QCD model by fitting the pseudocritical temperatures $T_{\mathrm{pc}(B)}$ from the lattice simulation [4]. Then, we numerically obtain the chiral condensates with different conditions of T and B and study their magnetic catalysis and inverse magnetic catalysis effects. In Sec. IV, we extract and investigate the longitudinal screening masses $m_{\mathrm{scr},\parallel}$, transverse screening masses $m_{\mathrm{scr},\perp}$, pole masses m_{pole}, and thermal widths $\Gamma/2$ of the neutral pion under finite temperature and magnetic field from the lattice-improved AdS/QCD model. Finally, in Sec. V, we give a summary and discussion.

II. GRAVITY BACKGROUND

For the gravity background, the authors in Ref. [74] employed an asymptotic expansion method to obtain an approximate solution of the Einstein-Maxwell (EM) system. However, the result is only reasonable under the condition $B \ll T^2$.[1] To extend to the large B region, we will introduce the "shooting method" [71,78] to solve the EM system and obtain its full solution.

To introduce the magnetic field, we follow the strategy in Refs. [74,79,80]. The backreaction of the magnetic field is

[1]In our study, the physical dimension of B is GeV^2.

considered in the EM system. Its action in five-dimensional space-time is

$$S_B = \frac{1}{16\pi G_5}\int d^5x\sqrt{-g}\left(R - F_{MN}F^{MN} + \frac{12}{L^2}\right), \quad (1)$$

with R the scalar curvature, L the AdS radius, and G_5 the 5D Newton constant. The notations M, N take values of $0, 1, \ldots, 4$. The g is the metric determinant of g_{MN}. The F_{MN} stands for a $U(1)$ gauge field. The matter part, described by the soft-wall AdS/QCD model, is considered as a probe on this background. Thus, the backreaction from the matter part is neglected.

A. EOMs within the EM system

Within the EM system, the equations of motion (EOMs) are

$$E_{MN} - \frac{6}{L^2}g_{MN} - \left(g^{IJ}F_{IM}F_{JN} - \frac{1}{4}F_{IJ}F^{IJ}g_{MN}\right) = 0, \quad (2a)$$

$$\nabla_M F^{MN} = 0, \quad (2b)$$

with E_{MN} the Einstein tensor, R_{MN} the Ricci tensor, and R the Ricci scalar: $E_{MN} = R_{MN} - \frac{R}{2}g_{MN}$. To satisfy the field equation for F_{MN} in Eq. (2b), the configuration of a constant magnetic field could be taken as

$$F = \frac{B}{L}dx_1 \wedge dx_2, \quad (3)$$

where L is set to unity in this work, $L = 1$.

In this 5D coordinate system, we have (t, x_1, x_2, x_3, z), in which the coordinate z corresponds to the radial holographic direction. For the magnetic field along the x_3 axis, one has $B_{x_3} = F_{x_1x_2} = \partial_{x_1}A_{x_2} - \partial_{x_2}A_{x_1} = B$, where the bulk gauge potential is defined as $A_\mu(x_1, z) = \frac{1}{2}B(x_1\delta_\mu^{x_2} - x_2\delta_\mu^{x_1})$. As a result, the metric ansatz could be chosen as

$$ds^2 = e^{2A(z)}\left(-f dt^2 + \frac{1}{f}dz^2 + h(dx_1^2 + dx_2^2) + q dx_3^2\right), \quad (4)$$

with $A(z) = -\ln(z)$. As our study focuses on the thermal properties in the equilibrium state, the f, h, and q are functions only with respect to the variable z.

Under the given metric ansatz in Eq. (4), the EOM in Eq. (2a) reduces to the following forms:

$$f'' + f'\left(\frac{h'}{3h} + \frac{q'}{6q} - \frac{3}{z}\right) + f\left(-\frac{2h'q'}{3hq} + \frac{2h'}{hz} - \frac{h'^2}{3h^2} + \frac{q'}{qz}\right) - \frac{8B^2z^2}{3h^2} = 0, \quad (5a)$$

$$q'' + q'\left(\frac{2f'}{3f} + \frac{h'}{3h} - \frac{2}{z}\right) + q\left(-\frac{8B^2z^2}{3fh^2} - \frac{2f'h'}{3fh} + \frac{2h'}{hz} - \frac{h'^2}{3h^2}\right) - \frac{q'^2}{2q} = 0, \quad (5b)$$

$$h'' + h'\left(\frac{f'}{3f} - \frac{q'}{6q} - \frac{1}{z}\right) + h\left(\frac{q'}{qz} - \frac{f'q'}{3fq}\right) - \frac{h'^2}{3h} + \frac{4B^2z^2}{3fh} = 0, \quad (5c)$$

together with a constraint equation

$$\frac{f'h'}{2fh} + \frac{f'q'}{4fq} - \frac{3f'}{2fz} - \frac{6}{fz^2} + \frac{h'q'}{2hq} - \frac{3h'}{hz} + \frac{h'^2}{4h^2} - \frac{3q'}{2qz} + \frac{6}{z^2} + \frac{B^2z^2}{fh^2} = 0. \quad (5d)$$

B. Complete numerical solutions

With a careful analysis of the EOMs in Eqs. (5), one can find that there are singularities at both $z = 0$ and $z = z_h$, which result in the difficulties in obtaining analytical solutions. Nevertheless, we can employ the numerical algorithm shooting method, as introduced in Refs. [71,78], to solve these ODEs.

For Eqs. (5), one can obtain the asymptotic expansions around the ultraviolet (UV) boundary at $z = 0$,

$$f(z) = 1 + \left(\frac{2B^2}{3h_0^2}\right)z^4\ln(z) + f_4z^4 + \mathcal{O}(z^5), \quad (6a)$$

$$q(z) = q_0 + \left(\frac{2q_0B^2}{3h_0^2}\right)z^4\ln(z) + q_4z^4 + \mathcal{O}(z^5), \quad (6b)$$

$$h(z) = h_0 - \left(\frac{B^2}{3h_0}\right)z^4\ln(z) - \frac{h_0q_4}{2q_0}z^4 + \mathcal{O}(z^5), \quad (6c)$$

with f_4, q_0, q_4, and h_0 the integration constants.

At the horizon $z = z_h$ or the infrared (IR) boundary, in order to get the black hole solution, the condition $f(z = z_h) = 0$ must be satisfied. Thus, for the asymptotic expansion of $f(z)$ at $z = z_h$, there is no constant term. Near the horizon, one can derive the asymptotic expansions of Eqs. (5) as

$$f(z) = f_{h1}(z - z_h) + \frac{1}{3z_h^2}\left(\frac{5B^2{z_h}^4}{h_{h0}^2} + 3z_hf_{h1} - 6\right) \times (z - z_h)^2 + \mathcal{O}(z - z_h)^3, \quad (7a)$$

$$
\begin{aligned}
q(z) = {}& q_{h0} + \frac{2q_{h0}}{3f_{h1}h_{h0}^2 z_h^2} \\
& \times (2B^2 z_h^4 + 3f_{h1}h_{h0}^2 z_h + 12h_{h0}^2)(z - z_h) \\
& + \frac{q_{h0}}{9{z_h}^4 f_{h1}^2 h_{h0}^4}[20B^4 {z_h}^8 + 12B^2 {z_h}^5 f_{h1} h_{h0}^2 \\
& + 9h_{h0}^4 (z_h f_{h1} + 4)^2](z - z_h)^2 + \mathcal{O}(z - z_h)^3, \quad (7b)
\end{aligned}
$$

$$
\begin{aligned}
h(z) = {}& h_{h0} + \frac{2}{3f_{h1}h_{h0}z_h^2} \\
& \times (-4B^2 z_h^4 + 3f_{h1}h_{h0}^2 z_h + 12h_{h0}^2)(z - z_h) \\
& + \frac{1}{9{z_h}^4 f_{h1}^2 h_{h0}^3}[8B^4 {z_h}^8 - 24B^2 {z_h}^4 h_{h0}^2 \\
& \times (z_h f_{h1} + 3) + 9h_{h0}^4 (z_h f_{h1} + 4)^2] \\
& \times (z - z_h)^2 + \mathcal{O}(z - z_h)^3, \quad (7c)
\end{aligned}
$$

where f_{h1}, q_{h0}, and h_{h0} are the integration constants.

Physically, when the magnetic field is absent, $B = 0$, the metric in Eq. (4) should reduce to

$$
dS^2 = \frac{L^2}{z^2}\left(-f dt^2 + \frac{1}{f}dz^2 + dx_1^2 + dx_2^2 + dx_3^2\right). \quad (8)
$$

This change stems from the restoration of isotropy within the spatial dimensions x_1, x_2, and x_3. From Eq. (8), it becomes evident that $h = q = 1$ at $B = 0$. By considering the zero magnetic field limit in the asymptotic expansions of Eq. (6), it is obvious that integral constants q_0 and h_0 should satisfy $q_0 = 1$ and $h_0 = 1$. Furthermore, the temperature is related to the horizon,

$$
T = \left|\frac{f'(z)}{4\pi}\right|_{z=z_h}. \quad (9)
$$

Thus, from Eqs. (7b) and (9), one can find that z_h is a function of B and T (or the temperature-related quantity f_{h1}).

Within this system, considering Eq. (5d), the number of constraints is reduced to 5. However, considering the asymptotic expansions of Eqs. (5) at $z = 0$ and $z = z_h$, the total amount of involved, unknown, integral constants is 5, including f_4 and q_4 at the $z = 0$ boundary, and f_{h1}, q_{h0}, and h_{h0} at the horizon.

In mathematics, within this EM system, the integral constants of the EM system and z_h should be clearly determined by the given values of B and f_{h1}. Thus, in our solving process, we treat f_4, q_4, q_{h0}, h_{h0}, and z_h as unknown quantities for any given B and temperature-related quantity f_{h1}.

To present how the temperature and magnetic field affect the background metric, we show variation curves of $f(z)$, $q(z)$, and $h(z)$ in Fig. 1. In Figs. 1(a)–1(c), without loss of generality, we choose that B is fixed at 1 GeV^2 as an example to check the temperature effects with $T \approx 0.008$, 0.159, and 0.398 GeV^2 in (a)–(c), respectively. We find that, as the temperature increases, the difference between $q(z)$ and $h(z)$ is vanishing, and both of them tend to unity. Considering the zero magnetic field limit metric in Eq. (4), this implies that an increase in temperature is beneficial for restoring the spatial rotation invariance broken by the magnetic field.[2] In Figs. 1(d)–1(f), we show the numerical results at fixed temperature $T \approx 0.398$ GeV to present the effect of the variation of the magnetic field. We observe that even at very high temperatures, $T \approx 0.398$ GeV, the curves of $q(z)$ and $h(z)$, which almost collapse at small B, become split as B increases. This indicates that an increase of the magnetic field enhances the spatial anisotropy. Therefore, there exists competition between the temperature and magnetic field for the spatial anisotropy of the background. On the one hand, increasing the magnetic field enhances the spatial anisotropy. On the other hand, increased temperature favors the restoration of spatial asymmetry.

Moreover, as shown in Figs. 1(g)–1(i), at very low fixed temperature $T \approx 8$ MeV, as B increases, $q(z)$ and $h(z)$ split while $f(z)$ and $q(z)$ converge. This suggests that at very low temperatures and large magnetic field, only slight differences exist between the temporal direction and the x_3 direction. According to the trend, it might be identical in the x_3 direction and the temporal one at $T = 0$. The physic in the x_3 direction and temporal one satisfy Lorentz rotation invariance. Moreover, in Ref. [21], it was argued that when $T = 0$, $B > 0$, there exist $m_{\mathrm{pole}} = m_{\mathrm{scr},\parallel}$. This is consistent with our deduction.

In Fig. 2(a), we show the T and B dependence of z_h, where the magnetic field B is from 0.01 GeV^2 to 4 GeV^2 and the temperature T is from 0.008 GeV to 0.4 GeV. Notably, at lower T and B, the value of z_h is significantly large. With increasing T and B, z_h undergoes a sharp decrease. Furthermore, we have a comparison to the perturbative asymptotic approximation results given in Ref. [74]. In Fig. 2(b), we present the relative error (RE) of z_h between full solutions and the perturbative asymptotic one. The comparison shows that the perturbative asymptotic approximation agrees well with the full solution outcomes in the region where $B \ll T^2$. Nevertheless, the deviations especially emerge in the region with low values of T and high values of B. Hence, when we study the low-temperature and high magnetic field regime, the full solution is necessary, and the asymptotic approximation is not suitable.

[2] In fact, in our calculations, no matter what value the B is fixed at, the temperature will always promote spatial isotropy. Physically, in higher temperature regions, the whole system will appear more chaotic. High temperatures lead to a large number of inelastic collisions, causing energy and momentum transfer between various degrees of freedom. Therefore, high temperatures are beneficial to "smoothen" the anisotropy brought by the magnetic field.

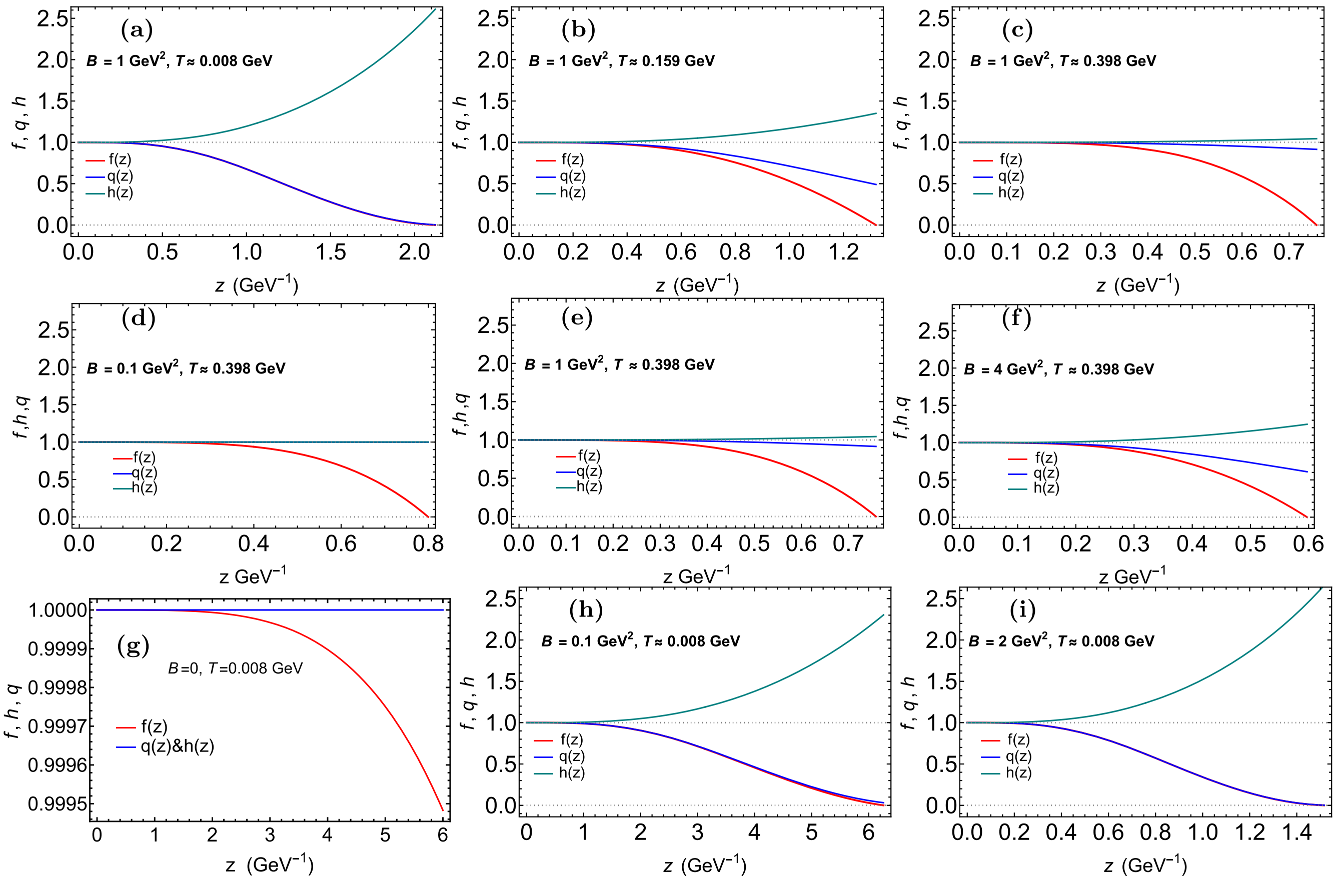

FIG. 1. The f, q, and h as functions of z represented by red, blue, and cyan lines, respectively. (a)–(c) Magnetic field B fixed at 1 GeV^2, with temperature T fixed at 8, 159, and 398 MeV, respectively. (d)–(f) Temperature T fixed at a high value, $T \approx 398$ MeV; magnetic field B fixed at 0.1, 1, and 4 GeV^2, respectively. (h),(i) Temperature T fixed at a low value, $T \approx 8$ MeV; magnetic field B fixed at 0, 0.1, and 2 GeV^2, respectively.

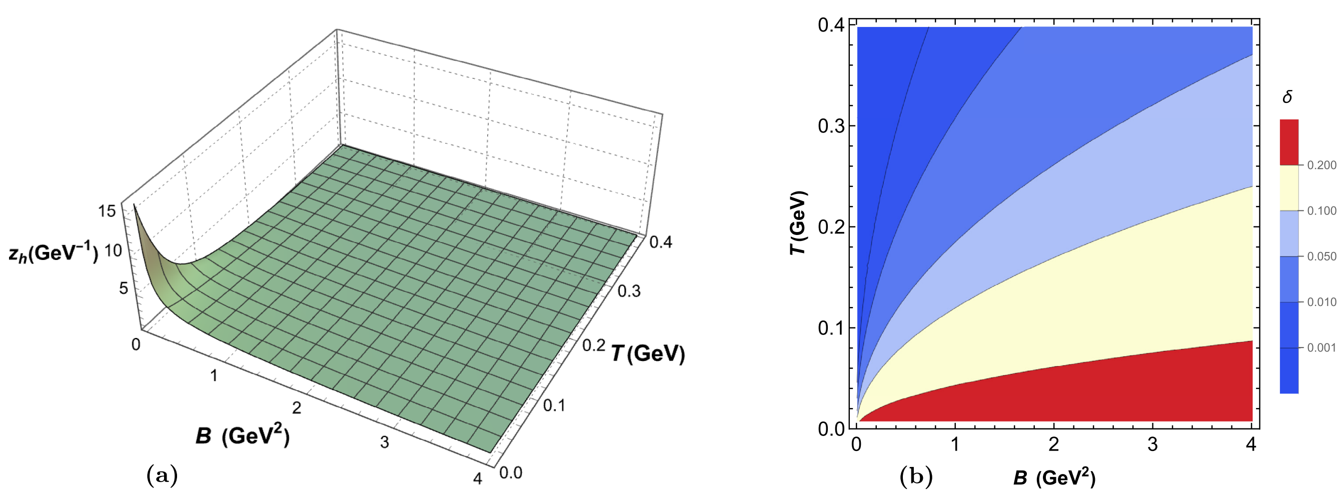

FIG. 2. (a) Horizon boundary z_h as a function of temperature T and magnetic field B. (b) Distribution of relative error of z_h, $\delta = \Delta/z_h = (z_h - \tilde{z}_h)/z_h$, with $\tilde{z}_h$ the perturbation result, between the results from the perturbative asymptotic approximation and the full solution across the plane of the temperature T and magnetic field B.

III. IMC AND MC EFFECTS ON CHIRAL PHASE TRANSITION

After obtaining the full solution for the EM system, we can explore the chiral phase transition through the order parameter (the chiral condensation). Among the various models investigating chiral phase transitions, the soft-wall model stands out as one of the most effective models. We investigate the chiral properties based on the soft-wall model.

In Ref. [74], chiral condensation exhibits noticeable IMC behavior, and its $T_{\rm pc}$ decreases with increasing eB. Under this model, we numerically calculate the full background solution and chiral condensation. The results indicate that no MC effect of chiral condensation exists at low temperatures. However, the LQCD simulations [4,18,23] suggest that chiral condensation should exhibit distinct MC and IMC behaviors at low temperatures and near $T_{\rm pc}$, respectively. The $T_{\rm pc}(B)$ monotonously decreases with the increase of B. Additionally, in the IR-improved soft-wall AdS/QCD model, the results indicate that the MC effects of chiral condensation at low temperatures are very weak [77]. Therefore, to more consistently describe the MC and IMC effects, it might be necessary to incorporate the magnetic field effects within the soft-wall model. Inspired by Ref. [22], we modify the 5D mass of the soft-wall AdS/QCD model by introducing a polynomial $g(B)$. The $g(B)$ is constrained by the variation of $T_{\rm pc}$ with B from lattice simulations [4]. In Ref. [73], they attempt to consider coupling between the dilaton Φ and scalar field X. Furthermore, in this work, we further optimize the AdS/QCD model by introducing a magnetic field-dependent polynomial $g(B)$ into an effective 5D mass expression.

The soft-wall AdS/QCD model is constructed within the bottom-up framework [41,42] by considering the $\mathrm{SU}(N_f)_L \times \mathrm{SU}(N_f)_R$ gauge symmetry. The action is expressed as

$$S_M = \int dz \int d^4x \sqrt{g} e^{-\Phi(z)} \mathrm{Tr}\Big\{ |DX|^2 - m_5^2(z)|X|^2 - \lambda |X|^4 - \frac{1}{4g_5^2}(F_L^2 + F_R^2) \Big\}, \tag{10}$$

with g the determinant of the metric g_{MN}. Note that $g_5 = 2\pi$, which is determined by comparing the large momentum expansion of the correlator of the vector current $J_\mu^a = \bar{q}\gamma_\mu t^a q$ in both AdS/QCD and perturbative QCD [41]. The dilaton profile $\Phi(z) = \mu_g^2 z^2$, with μ_g the constant necessary for the Regge behavior of the meson spectrum [42]. The covariant derivative D^M and the field strength $F_{L,R}^{MN}$ are defined as $D^M X = \partial^M X - iA_L^M X + iXA_R^M$ and $F_{L,R}^{MN} = \partial^M A_{L,R}^N - \partial^N A_{L,R}^M - i[A_{L,R}^M, A_{L,R}^N]$, with $A_{L,R}^M = A_{L,R}^{a,M} t_{L,R}^a$. The $t_{L,R}^a$ ($a = 1, 2, 3$) is defined as the generator of $\mathrm{SU}(2)_L$ and $\mathrm{SU}(2)_R$, respectively, with $M, N = 0, 1, 2, 3, 4$. In this work, we only consider the case of $N_f = 2$ with equal u and d quark mass, $m_q = m_u = m_d$.

TABLE I. Parameters of the model.

Parameters	m_q (GeV)	μ_g (GeV)	κ	γ	λ
Value	3.90×10^{-3}	0.35	0.85	6	25

For the sake of convenience, the gauge field $A_{L/R}$ can generally be rearranged into the vector field $V^M = \frac{1}{2}(A_L^M + A_R^M)$ and the axial-vector field $A^M = \frac{1}{2}(A_L^M - A_R^M)$. The vector field V^M corresponds, as dual entities, to the vector current J_μ^V. The axial-vector field A^M corresponds, as dual entities, to the axial-vector current J_μ^A. The accompanying transformed chiral gauge field strengths are denoted as

$$F_A^{MN} = \frac{1}{2}(F_L^{MN} - F_R^{MN}) = \partial^M A^N - \partial^N A^M - i[V^M, A^N] - i[A^M, V^N], \tag{11a}$$

$$F_V^{MN} = \frac{1}{2}(F_L^{MN} + F_R^{MN}) = \partial^M V^N - \partial^N V^M - i[V^M, A^N] - i[A^M, V^N]. \tag{11b}$$

Furthermore, the covariant derivative is

$$D_M X = \partial_M X - i[V_M, X] - i\{A_M, X\}. \tag{11c}$$

Considering the coupling between the scalar field X and the dilaton Φ $m_5^2(z)$ effectively leads to the modification of m_5,

$$m_5^2(z) = -3[1 + \gamma \tanh(\kappa\Phi)], \tag{12}$$

with γ, κ the free parameters. The leading constant term for the 5D mass, denoted as $m_5^2 = -3$, can be established by the AdS/CFT dictionary: $m_5^2 = (\Delta - p)(\Delta + p - 4)$, with the choice of $p = 0$ and $\Delta = 3$, where Δ represents the dimension of the dual operator $\bar{q}_R \bar{q}_L$ [41].

In Ref. [73], the chiral condensation has slight unphysical increases in the low temperature region with increasing temperature, so the model parameters should be adjusted. Our goal is to achieve the pion mass M_π,[3] $M_\pi \approx 139.6$ (MeV) [81], and the saturation chiral condensate σ, $\sigma \approx 0.0278$ (GeV^3) [51]. Details of the new parameters are provided in Table. I. The selection and adjustment of parameters involve the following steps. Initially, we

[3]The uppercase M_π in this article specifically denotes the mass of the π meson under conditions of zero temperature, zero density, and zero magnetic field strength.

adjusted the value of μ_g, a parameter associated with the Regge behavior of the meson spectrum, and fixed it at 0.35 GeV. Subsequently, we adjusted the magnitude of λ, which directly influenced the value of the chiral condensation σ, setting it to 25. Finally, we determined the values of κ and γ. In our parameter tuning, we found that the values of κ and γ not only affect the $T_{\rm pc}$ but also impact the magnitude of σ. In the absence of an external magnetic field, given that the pseudocritical temperature $T_{\rm pc}$ should lie between 150 and 170 MeV, we fit $\kappa = 0.85$ and $\gamma = 6$. Additionally, as the quark mass m_q is positively correlated with M_π, we fit m_q to 3.9 MeV. The computed result with these parameters yields the pseudocritical temperature $T_{\rm pc}(B=0) \approx 161$ MeV.

Furthermore, during the parameter adjustment process, we observed that changing the coefficient of the dilation function $\Phi(z)$ in Eq. (12) alone could affect both the values of σ and $T_{\rm pc}$. Therefore, when introducing the magnetic field-dependent function $g(B)$ into the effective 5D mass in Eq. (12), we have $\kappa + g(B)$ as the coefficient of the dilation $\Phi(z)$. Finally, to make the coefficient dimensionless, we have reduced B as B/μ_g^2. After incorporating the magnetic field-dependent polynomial $g(B)$, the expression for the effective 5D mass becomes

$$m_5^2(z) = -3\{1 + \gamma \tanh[(\kappa + g(B))\Phi]\}, \tag{13}$$

where

$$g(B) = \sum_i \eta_i \left(\frac{B}{\mu_g^2}\right)^{\alpha_i}, \tag{14}$$

with $\alpha_i = 2, 4, 6, 8, 10$. Since the magnitude of chiral condensation should not be impacted by the direction of the magnetic field, we set all α_i to be even. In order to ensure that the variation of $T_{\rm pc}(B)$ falls entirely within the error band of the LQCD result, we adjust $g(B)$ based on the $T_{\rm pc}$ data points extracted from LQCD simulations [4]. Furthermore, we observe that it is different in M_π and $T_{\rm pc}(B=0)$ for different effective models. Thus, we opt to use a dimensionless quantity B/M_π^2 to measure the strength of the magnetic field. We also use the normalized pseudocritical temperature $T_{\rm pc}(B)/T_{\rm pc}(B=0)$ to assess the variation in the pseudocritical temperature with B. Finally, we obtain the fitted coefficients as shown in Table II.

In the $N_f = 2$ case, with equal u and d quark mass, $m_q = m_u = m_d$, the bulk scalar field X can be expressed as

TABLE II. Coefficients of η_i.

η_1	η_2	η_3	η_4	η_5
0.021	-8.65×10^{-4}	2.02×10^{-5}	-2.37×10^{-7}	1.10×10^{-9}

$$X = \left(\frac{\chi}{2} + S\right) I_2 e^{2i\pi^a t^a}, \tag{15}$$

where $\chi(z)$ is linked to the vacuum expectation value (VEV) of X and I_2 represents the 2×2 identity matrix. Therefore, one can derive the EOM for χ as

$$\chi'' + \left(3A' - \Phi' + \frac{f'}{f} + \frac{h'}{h} + \frac{q'}{2q}\right)\chi' - \frac{e^{2A}\chi(\lambda\chi^2 + 2m_5^2)}{2f} = 0. \tag{16}$$

The EOM for χ in Eq. (16) is a nonlinear second-order differential equation with singularities at both $z = 0$ and $z = z_h$, which makes analytical solutions difficult to attain. Nevertheless, we can numerically solve it with an algorithm (shooting method) as utilized in Ref. [71]. Within this algorithm, by considering Eqs. (II A), we can derive the asymptotic expansions of χ at both the UV and IR boundaries as

$$\chi(z \to 0) = m_q\zeta z + \frac{\sigma}{\zeta} z + \frac{1}{4} m_q \zeta[-6\gamma\mu_g^2 g(B) + (4 - 6\gamma\kappa)\mu_g^2 + \lambda\zeta^2 m_q^2] z^3 \ln(z) + \mathcal{O}(z^4), \tag{17a}$$

$$\chi(z \to z_h) = \chi_{zh0} + \frac{1}{2f_{h1}z_h^2}\chi_{zh0}\{\lambda\chi_{zh0}^2 - 6 - 6\gamma \times \tanh[(\kappa + g(B))\mu_g^2 z_h^2]\}(z - z_h) + \mathcal{O}(z - z_h)^2, \tag{17b}$$

with integration constants m_q, σ, and χ_{zh0}. According to the holographic dictionary, the two integral constants, m_q and σ, correspond to the quark mass and the chiral condensate $\sigma \equiv \langle \bar{q}q \rangle$, respectively. Furthermore, the normalization constant ζ takes the value $\sqrt{N_c}/2\pi$ with $N_c = 3$, which is determined by matching to 4D QCD [82].

In Fig. 3, we show the variation of chiral condensation with T (or B) when B (or T) is fixed. In Fig. 3(a), under different fixed B and varying T, the chiral phase transition exhibits crossover behavior. The results suggest that chiral condensation displays evident MC effects at low temperatures and significant IMC effects near $T_{\rm pc}(B)$. From Fig. 3(b), we observe that chiral condensation exhibits MC effects at low temperature. As the temperature increases to 140 MeV, chiral condensation initially shows MC behavior. Then, when the magnetic field strength B is at $B \gtrsim 34\ M_\pi^2$, the behavior of the chiral condensation transition shifts from the MC to the IMC effect. Finally, when the temperature reaches 162 MeV, chiral condensation completely manifests IMC effects. These findings are qualitatively consistent with lattice simulation results [4,18]. On the other hand, when the temperature is at $T \gtrsim 201$ MeV,

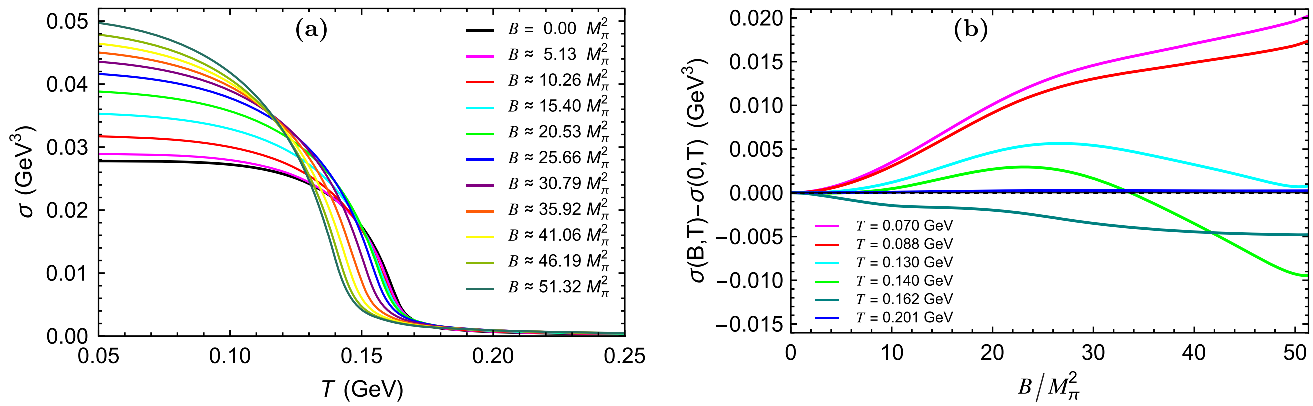

FIG. 3. (a) Chiral condensation σ as a function of T under different fixed B. The range of B is approximately from 0 to 51.32 M_π^2, which corresponds to 0 to 1 GeV^2 in our model. (b) $\Delta\sigma = \sigma(B,T) - \sigma(0,T)$ as a function of B/M_π^2 under different fixed T, where the temperatures T are chosen as 70, 88, 130, 140, 162, and 201 MeV, respectively.

the variation of $\Delta\sigma$ is almost decoupled from the magnetic field.

As shown in Fig. 4, we have also derived the results for the normalized pseudocritical temperature $T_{\mathrm{pc}}(B)/T_{\mathrm{pc}}(0)$. The pseudocritical temperature is defined as $(\partial^2\sigma/\partial T^2)|_{T=T_{\mathrm{pc}}} = 0$. We can observe that the normalized $T_{\mathrm{pc}}(B)$ results fall entirely within the error band of lattice simulations [4]. Additionally, we extracted results of T_{pc} from the lattice-improved NJL model [22] for comparison.

IV. CORRELATION FUNCTIONS AND MASSES OF NEUTRAL PION AT FINITE TEMPERATURE AND MAGNETIC FIELD

In the previous section, we constructed the lattice-improved soft-wall AdS/QCD model. We used this model to study the chiral condensate and the chiral phase transition. In this section, we focus on the calculation of the screening masses m_{scr}, the pole masses m_{pole}, and the thermal widths Γ of the neutral pion π^0 under different magnetic field strengths B and temperatures T.

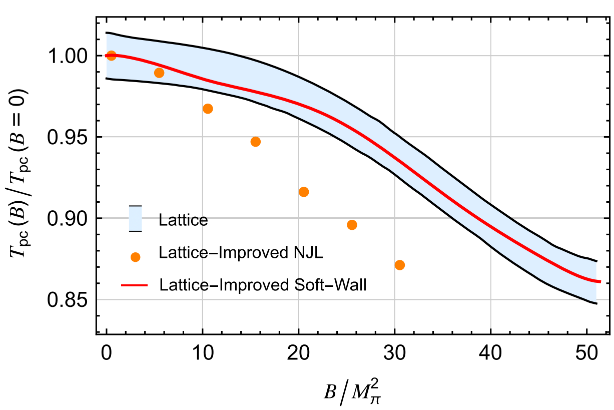

FIG. 4. Pseudocritical temperature scaled by its $B = 0$ value as a function of B/M_π^2. These results compare with those from lattice simulations [4] and lattice-improved NJL [22]. Given that the values of M_π in lattice simulations and the lattice-improved NJL model are 135 and 138 MeV, respectively, the results have been scaled accordingly for their respective M_π in the extracted data.

The screening mass m_{scr} describes the exponential decay of the spatial correlator $G(\vec{x}) \sim e^{-m_{\mathrm{scr}}|\vec{x}|}/|\vec{x}|$. In other words, it is the pole in the momentum space, while the correlation function has the following form near the pole:

$$G(0,\boldsymbol{k}) \sim \frac{1}{\boldsymbol{k}^2 + m_{\mathrm{scr}}^2}. \tag{18}$$

Besides the spatial components, the information about the temporal component is also important to obtain a full understanding of the mesonic correlation. It is described by the pole mass and the thermal width. These both appear in the pole in the complex frequency plane, near which the temporal correlation function takes the form

$$G(k_0,\mathbf{0}) \sim \frac{1}{k_0 - (m_{\mathrm{pole}} - i\Gamma/2)}. \tag{19}$$

Here, we take the four-vector k as $k = (k_0, \boldsymbol{k})$, and $k_0, \boldsymbol{k}$ represent the frequency and the spatial momentum, respectively.

Thus, to obtain those quantities, one has to calculate the correlators. Through the holographic approach, a linkage is forged between the 4D operator $\hat{O}(x)$ and the 5D field $\phi_0(x,z)$ by equating their partition functions. This methodology stands as a robust means to tackle strong coupling correlation functions,

$$\langle e^{i\int d^4x \phi_0(x)\hat{O}(x)}\rangle = e^{iS_{5D[\phi]}}|_{\phi(x,z=0)=\phi_0(x)}, \tag{20}$$

with the field ϕ, which corresponds to the classical solution of the 5D action S_{5D}. The boundary value $\phi(x,z=0)$ corresponds to the 4D external source $\phi_0(x)$ [38–40] within 5D space. By taking the second derivative of the action S_{5D}

with respect to the source ϕ_0, the correlator $\langle \hat{O}(x)\hat{O}(0)\rangle$ can be calculated [83]. In this way, it is possible to obtain the poles of the correlation functions and the masses. However, as mentioned in Ref. [71], the poles can be easily obtained by solving the 5D equations of motion under certain boundary conditions. In this way, one can obtain the screening mass by solving the equations of motion with a spatial momentum while replacing the spatial momentum with frequency for pole mass and thermal width. For details, refer to Ref. [71].

Note that those screening and pole masses are not independent; they are connected by the dispersion relation. Generally, within a thermal medium in an external magnetic field, the dispersion relation is represented by

$$k_0^2 = u_\perp^2 \boldsymbol{k}_\perp^2 + u_\parallel^2 \boldsymbol{k}_\parallel^2 + m_{\text{pole}}^2, \tag{21}$$

where we denote $u_\perp = u_1 = u_2$ and $u_\parallel = u_3$ the velocities of transverse and longitudinal directions, respectively. The transverse directions are in the x_1, x_2 directions, and the longitudinal direction is in the x_3 direction, along the magnetic field. Note that $\boldsymbol{k}_\perp$ and $\boldsymbol{k}_\parallel$ are the transverse and longitudinal momenta, respectively. Furthermore, u_i represents the pion sound velocity in the x_i direction. Therefore, $m_{\text{scr},\perp}$ and $m_{\text{scr},\parallel}$ can be defined in terms of m_{pole} and the velocity of sound in that direction, as $m_{\text{scr},\perp} = \frac{m_{\text{pole}}}{u_\perp}$ and $m_{\text{scr},\parallel} = \frac{m_{\text{pole}}}{u_\parallel}$. As discussed in Refs. [21,33], effective thermal masses will lead to $u_\perp < 1$ and $u_\parallel < 1$. Note also that transversal thermal motion is not as strong as longitudinal motion due to the dimensional reduction of the magnetic field, giving $u_\perp < u_\parallel$. Finally, we have $m_{\text{scr},\perp} > m_{\text{scr},\parallel} > m_{\text{pole}}$.

After the above preparation, in the following subsections we will derive the EOMs and their asymptotic expansions in the pseudoscalar channel. Then, we will extract the masses and present the numerical results of $m_{\text{scr},\perp}$, $m_{\text{scr},\parallel}$, and m_{pole}. In addition, $u_\perp/u_\parallel$ will be examined as it serves to measure the anisotropy induced by the magnetic field.

A. EOMs and their asymptotic expansion of the pseudoscalar channel

As the scalar meson fields $S(\chi, z)$ and $\pi(\chi, z)$ are decoupled, $S(\chi, z)$ can be set to zero. The expression of X in Eq. (15) is reduced to

$$X = \frac{1}{2}\chi I_2 e^{2i\pi^a t^a}. \tag{22}$$

Moreover, the interaction between the pion field and the longitudinal component φ^i of the axial-vector field a^i occurs exclusively in the pseudoscalar channel. To simplify our analysis, we will adopt the following decomposition of the gauge field, for convenience:

$$a_\mu^i = a_\mu^{T,i} + \partial_\mu \varphi^i, \tag{23a}$$

$$\partial^\mu a_\mu^{T,i} = 0. \tag{23b}$$

When obtaining the EOMs within our model, we treat the π^0 meson as a perturbation and therefore neglect terms beyond quadratic order. Additionally, we adopt $A_z = 0$. By combining Eqs. (10), (22), and (23) and taking the Fourier transformation,

$$\pi^a(x, z) = \frac{1}{(2\pi)^4}\int dk^4 e^{-ikx}\pi^a(k, z), \tag{24a}$$

$$\varphi^a(x, z) = \frac{1}{(2\pi)^4}\int dk^4 e^{-ikx}\varphi^a(k, z), \tag{24b}$$

we derive the EOMs governing the behavior of the neutral π^0 meson and φ,

$$\partial_z(\sqrt{g}e^{-\Phi}g^{zz}\chi^2\partial_z\pi) - k_\mu^2\sqrt{g}e^{-\Phi}g^{\mu\mu}\chi^2(\pi - \varphi) = 0, \tag{25a}$$

$$\partial_z(\sqrt{g}e^{-\Phi}g^{zz}g^{\mu\mu}\partial_z\varphi) - g_5^2\sqrt{g}e^{-\Phi}g^{\mu\mu}\chi^2(\pi - \varphi) = 0, \tag{25b}$$

where k_μ represents the momenta of the neutral pion meson in the temporal and different spatial directions with $\mu = t, x_1, x_2, x_3$.

From Eqs. (25), since the x_1 and x_2 directions are perpendicular to the magnetic field, the x_1 and x_2 (transverse) directions possess isotropic properties. Clearly, for the spatial x_1 and x_2 directions, the system of differential equations is

$$\varphi'' + \left(A' + \frac{f'}{f} + \frac{q'}{2q} - \Phi'\right)\varphi' + \frac{e^{2A}g_5^2\chi^2}{f}(\pi - \varphi) = 0, \tag{26a}$$

$$\pi'' + \left(3A' + \frac{f'}{f} + \frac{q'}{2q} + \frac{h'}{h} - \Phi' + \frac{2\chi'}{\chi}\right)\pi' - \frac{k_1^2}{fh}(\pi - \varphi) = 0. \tag{26b}$$

Similarly, in the x_3 spatial (longitudinal) direction, the system of differential equations for π and φ is

$$\varphi'' + \left(A' + \frac{f'}{f} - \frac{q'}{2q} + \frac{h'}{h} - \Phi'\right)\varphi' + \frac{e^{2A}g_5^2\chi^2}{f}(\pi - \varphi) = 0, \tag{27a}$$

$$\pi'' + \left(3A' + \frac{f'}{f} + \frac{q'}{2q} + \frac{h'}{h} - \Phi' + \frac{2\chi'}{\chi}\right)\pi' - \frac{k_3^2}{fq}(\pi - \varphi) = 0. \tag{27b}$$

In the temporal direction, the system of differential equations for π and φ is

$$\varphi'' + \left(A' + \frac{h'}{h} + \frac{q'}{2q} - \Phi'\right)\varphi' + \frac{e^{2A} g_5^2 \chi^2}{f}(\pi - \varphi) = 0, \tag{28a}$$

$$\pi'' + \left(3A' + \frac{f'}{f} + \frac{q'}{2q} + \frac{h'}{h} - \Phi' + \frac{2\chi'}{\chi}\right)\pi' + \frac{k_0^2}{f^2}(\pi - \varphi) = 0. \tag{28b}$$

To solve Eqs. (26)–(28), we can also adopt the shooting method. This numerical approach enables us to tackle these differential equations effectively. In our numerical solution process, we start by establishing the asymptotic expansions of the equations at their respective boundaries $z = 0$ and $z = z_h$.[4] At the horizon, one should consider the incoming wave condition [84]. For the spatial direction along x_1 and x_2, the asymptotic expansion of Eqs. (26) at both boundaries can be described as

$$\pi(z \to 0) = \pi_{b0} + \varphi_0 + \pi_2 z^2 + \frac{\pi_{b0} k_1^2}{2h_0} z^2 \ln(z) + \mathcal{O}(z^3), \tag{29a}$$

$$\varphi(z \to 0) = \varphi_0 + \varphi_2 z^2 - \frac{1}{2} g_5^2 m_q^2 \zeta^2 \pi_{b0} z^2 \ln(z) + \mathcal{O}(z^3), \tag{29b}$$

$$\pi(z \to z_h) = \pi_{h0} + \frac{\pi_{h0} - \varphi_{h0}}{f_{h1} h_{h0}} k_1^2 (z - z_h) + \mathcal{O}(z - z_h)^2, \tag{29c}$$

$$\varphi(z \to z_h) = \varphi_{h0} + \frac{\varphi_{h0} - \pi_{h0}}{f_{h1} z_h^2} g_5^2 \chi_{zh0}^2 (z - z_h) + \mathcal{O}(z - z_h)^2, \tag{29d}$$

where π_{b0}, φ_0, π_2, and φ_2 are the integration constants for the UV boundary, and π_{h0} and φ_{h0} are the integration constants for the horizon.

[4]Because the metric functions and χ exist in Eqs. (26)–(28), when seeking their asymptotic expansions at the UV and IR boundaries, we must also take into account the asymptotic expansions of Eqs. (5) and (16) at the UV and IR regimes, respectively.

For the EOMs in the longitudinal direction (x_3 direction), we can obtain the asymptotic expansions of Eqs. (27) at both boundaries as

$$\pi(z \to 0) = \pi_{b0} + \varphi_0 + \pi_2 z^2 + \frac{\pi_{b0} k_3^2}{2q_0} z^2 \ln(z) + \mathcal{O}(z^3), \tag{30a}$$

$$\varphi(z \to 0) = \varphi_0 + \varphi_2 z^2 - \frac{1}{2} g_5^2 m_q^2 \zeta^2 \pi_{b0} z^2 \ln(z) + \mathcal{O}(z^3), \tag{30b}$$

$$\pi(z \to z_h) = \pi_{h0} + \frac{\pi_{h0} - \varphi_{h0}}{f_{h1} q_{h0}} k_3^2 (z - z_h) + \mathcal{O}(z - z_h)^2, \tag{30c}$$

$$\varphi(z \to z_h) = \varphi_{h0} + \frac{\varphi_{h0} - \pi_{h0}}{f_{h1} z_h^2} g_5^2 \chi_{zh0}^2 (z - z_h) + \mathcal{O}(z - z_h)^2, \tag{30d}$$

where π_{b0}, φ_0, π_2, and φ_2 are the integration constants for the UV boundary, and π_{h0} and φ_{h0} are the integration constants for the horizon.

Similarly, in the temporal direction, we can obtain the asymptotic expansion of Eqs. (28) at both boundaries, given by

$$\pi(z \to 0) = \pi_{b0} + \varphi_0 + \pi_2 z^2 - \frac{\pi_{b0} k_0^2}{2} z^2 \ln(z) + \mathcal{O}(z^3), \tag{31a}$$

$$\varphi(z \to 0) = \varphi_0 + \varphi_2 z^2 - \frac{1}{2} g_5^2 m_q^2 \zeta^2 \pi_{b0} z^2 \ln(z) + \mathcal{O}(z^5), \tag{31b}$$

$$\pi(z \to z_h) = \varphi_{h0} + (z - z_h)^{\frac{ik_0}{f_{h1}}} [\pi_{h0} + \mathcal{O}(z - z_h)^1], \tag{31c}$$

$$\varphi(z \to z_h) = \varphi_{h0} + (z - z_h)^{\frac{ik_0}{f_{h1}}} \times \left[\frac{i g_5^2 \pi_{h0} f_{h1} \chi_{zh0}^2}{{z_h}^2 k_t (f_{h1} + i k_t)} (z - z_h) + \mathcal{O}(z - z_h)^2\right]. \tag{31d}$$

The π_{b0}, φ_0, π_2, and φ_2 are the integration constants for the UV boundary, and φ_{h0} and π_{h0} are the integration constants for the horizon.

As explained in Ref. [72], due to the presence of the term $(\pi - \varphi)$ in Eqs. (25), if one makes a transformation assuming $\pi_c = \pi + c$ and $\varphi_c = \varphi + c$ with c a nonzero constant, one finds that the solution is still available. Consequently, we can take the integration constant φ_0 as

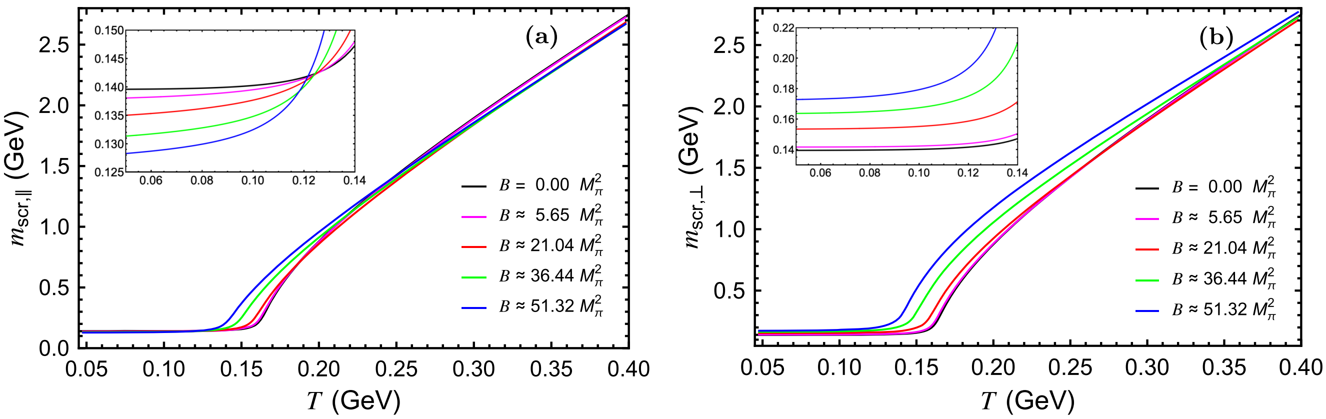

FIG. 5. The $m_{\mathrm{scr},\parallel}$ and $m_{\mathrm{scr},\perp}$ as a function of T under different fixed B, respectively. The fixed magnetic field B is about 0, 5.56, 21.04, 36.44, and 51.32 M_π^2, which corresponds to 0, 0.11, 0.41, 0.71, and 1 GeV^2, respectively, in our model. The inset in (a) and (b) is a zoom for the range $T \in [0.05, 0.14]$ GeV. For $B = 0$, 5.56, 21.04, 36.44, and 51.32 M_π^2, their corresponding T_{pc} of the chiral phase transition are 161.0, 160.2, 156.0, 146.5, and 138.8 MeV, respectively.

an extraneous free parameter. For convenience, we let $\varphi_0 = 0$. Additionally, due to the linear nature of Eqs. (25), for the integral constants π_{h0} at the IR boundary, we can set it to unity.

With the asymptotic expansion solutions, we can use the shooting method to numerically solve the differential system of equations (25) for π and φ. Because of the second-order differential equations, one should match the function's values and its first-order derivatives. Therefore, there are four constraints. However, as per the analysis presented above, the integration constants that we need to solve are π_{b0} π_2, φ_2, φ_{h0}, and k_i for each direction. However, physically analyzing the solutions of the differential equations and the two-point retarded correlator allows us to determine another integration constant, π_{b0}, for each direction, which will be explored and discussed in the subsequent subsections.

B. Numerical results of screening masses of the neutral pion

In this subsection, we will proceed to numerically solve the EOMs for π and φ, Eqs. (26) and (27). Then, we will show the transverse and longitudinal screening masses of the neutral pion.

Following the holographic dictionary, π_{b0}, as shown in the asymptotic expansions in Eqs. (29) and (30), is interpreted as the external source J_π. In fact, considering the spatial correlator in Eq. (18), the desired value of $m_{\mathrm{scr},\perp}$ or $m_{\mathrm{scr},\parallel}$ for the neutral pion meson is situated at the pole of the Green's function, representing its singularities. Consequently, at the UV boundary, the integral constants π_{b0} in the asymptotic expansion can be set to zero [72,73]. Thus, $m_{\mathrm{scr},\perp}$ and $m_{\mathrm{scr},\parallel}$ are the imaginary parts of k_1 and k_3.

After numerically solving the EOMs of π and φ in different directions by combining Eqs. (II A) and (16), we show the solution of the screening mass of the neutral pion in Figs. 5 and 6.

The behavior of the screening masses with respect to T at different fixed B is shown in Fig. 5. At low temperature, $m_{\mathrm{scr},\parallel}$ and $m_{\mathrm{scr},\perp}$ are both slightly affected by T. As shown in the inset, $m_{\mathrm{scr},\parallel}$ and $m_{\mathrm{scr},\perp}$ show decreasing and increasing behaviors with B in the low temperature region. In the critical region, close to $T_{\mathrm{pc}}(B)$, both screening masses suddenly increase. As the temperature increases, the two screening masses are characterized by the linear thermal mass and tend to be the same for different B at extremely high temperatures.

In Fig. 6, we plot the normalized screening mass of neutral pion mesons with B at different fixed T. As shown, the normalized screening masses ($m_{\mathrm{scr},\parallel}$ and $m_{\mathrm{scr},\perp}$), either at low ($T = 70$) MeV or at higher temperatures ($T = 212$ and 398 MeV), depend slightly on B, which corresponds to the main properties of a neutral particle. More precisely, at $T = 70$ MeV, $m_{\mathrm{scr},\parallel}$ decrease with increasing B, but $m_{\mathrm{scr},\perp}$ increase with increasing B. At $T = 212$ MeV, $m_{\mathrm{scr},\parallel}$ first decreases and then starts to increase as B grows. They both always increase with B when the temperature is $T < 398$ MeV. At a higher given temperature, $T = 398$ MeV, $m_{\mathrm{scr},\parallel}$ again decreases with B, and the decrease is very small. This is in agreement with the lattice result [23]. However, at a certain temperature where $T = 158$ MeV near $T_{\mathrm{pc}}(B)$, the normalized screening masses increase significantly with B, which can be understood as the magnetic dependence being enhanced by the critical fluctuation.

From the energy dispersion relation in Eq. (21), it is known that $u_\perp/u_\parallel = m_{\mathrm{scr},\parallel}/m_{\mathrm{scr},\perp}$. In Fig. 7(a), we present the T dependence of the ratio $u_\perp/u_\parallel$ at different eB. For finite eB, $u_\perp/u_\parallel$ is almost independent of temperature at low T. As the temperature increases to near $T_{\mathrm{pc}}(B)$, $u_\perp/u_\parallel$

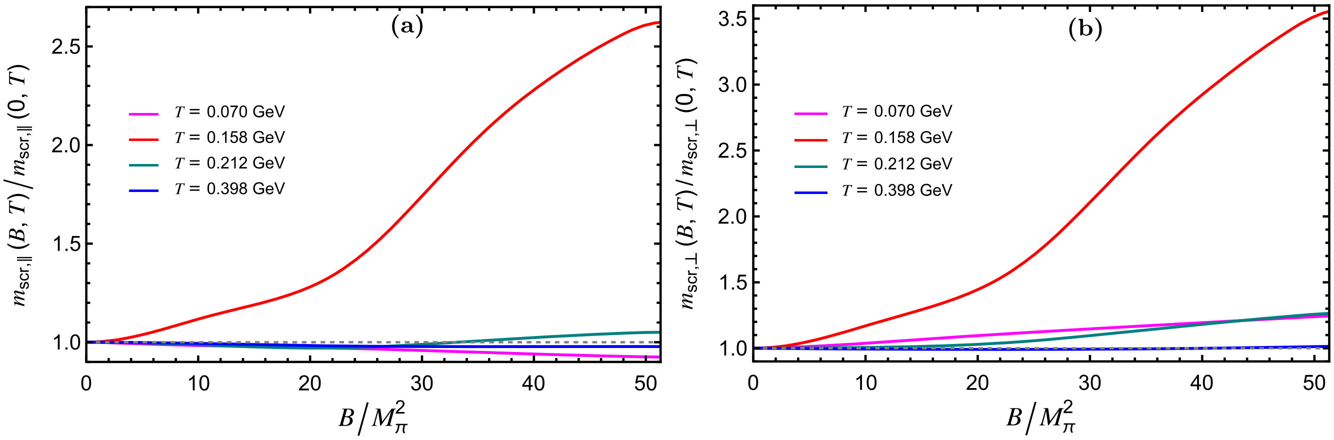

FIG. 6. Normalized screening mass, $m_{\mathrm{scr}}(B,T)/m_{\mathrm{scr}}(0,T)$, as a function of B/M_π^2 under different fixed T, where the temperatures T are chosen as 70, 158, 212, and 398 MeV, respectively. Panels (a) and (b) show normalized screening masses in the longitudinal and transverse screening masses, respectively.

shows a nonmonotonic bump, and the bump is more obvious as eB increases. When the temperature is $T > T_{\mathrm{pc}}(B)$, all curves increase with increasing T. When $T \gg T_{\mathrm{pc}}(B)$, all curves approach 1. Mathematically, increasing T will cause both $q(z)$ and $h(z)$ to approach 1, as shown in Sec. II B; then, we find that Eq. (26) is almost the same as Eq. (27). This indicates that in all three spatial dimensions, the thermal fluctuations dominate over the anisotropy induced by the magnetic field. Furthermore, in Fig. 7(b), we study the B dependence of the ratio $u_\perp/u_\parallel$. The ratio $u_\perp/u_\parallel$ decreases with increasing B, which is the consequence of the decoupling of the transverse dimension in the strong limit of the magnetic field. Again, in the region of critical temperature, the curve decays faster with B, as expected, as shown by the orange line.

C. Numerical results of pole mass and thermal widths of the neutral pion

In this subsection, we present the behavior of the pole mass m_{pole} and thermal width $\Gamma/2$ of the neutral pion meson at given T and B.

For asymptotic expansion in Eq. (31), according to the holographic dictionary, the integration constant π_{b0} is understood to correspond to the external sources denoted as J_π. From the temporal correlator, Eq. (19), we know that the complex frequencies k_0 precisely lie in the location of the poles in the Green's function. Evidently, this corresponds exactly to the position of singularities. Thus, for the integration constant π_{b0}, its value must be zero [72,73]. Hence, taking into account the analysis from Sec. IV A, we have already determined that $\varphi_0 = 0$, $\pi_{b0} = 0$, and

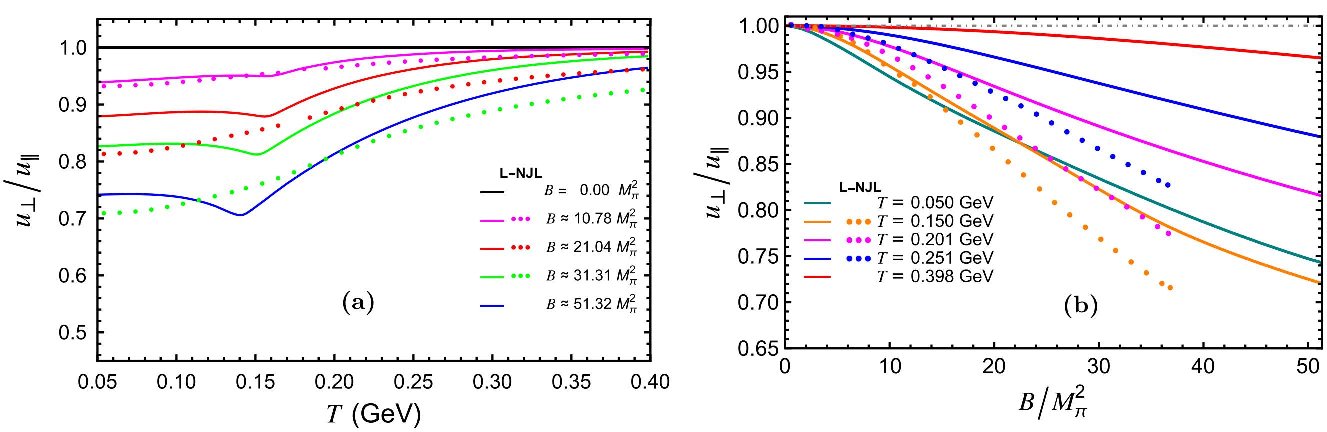

FIG. 7. (a) Ratio of sound velocity $u_\perp/u_\parallel$ as a function of T under different fixed B. The range of B is approximately from 0 to 51.32 M_π^2, which corresponds to 0 to 1 GeV^2 in our model. (b) Ratio of sound velocity $u_\perp/u_\parallel$ as a function of B/M_π^2 under different fixed T, where the temperatures T are chosen as 50, 150, 201, 251, and 398 MeV, respectively. For $B = 0$, 10.78, 21.04, 31.31, and 51.32 M_π^2, the corresponding T_{pc} of the chiral phase transition are 161.0, 158.7, 156.1, 150.2, and 138.8 MeV, respectively. Furthermore, we have extracted results from the lattice-improved NJL model [22], represented by dots in the graph. The displayed results from the lattice-improved NJL model have been scaled according to M_π of the model, $M_\pi = 138$ MeV.

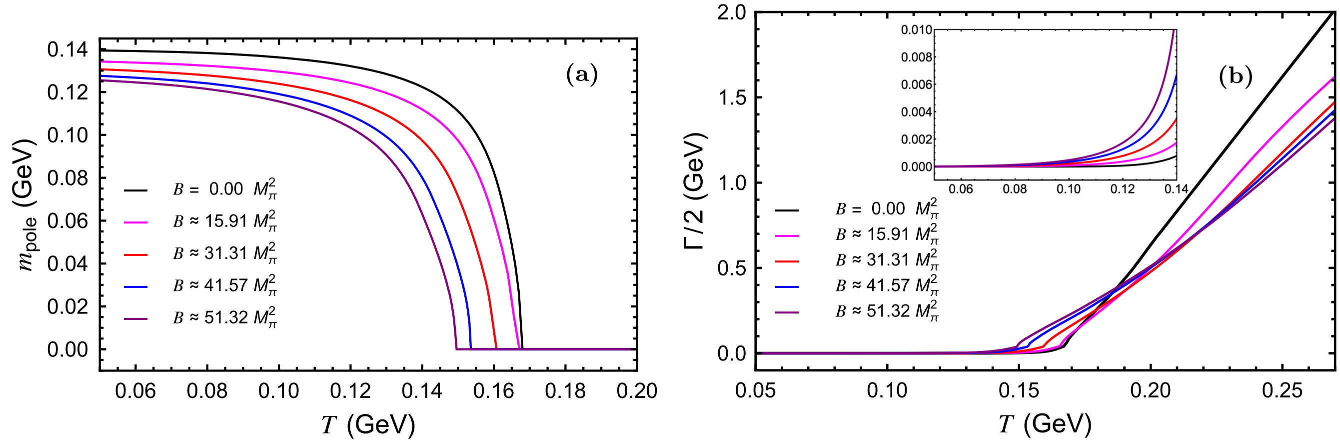

FIG. 8. Illustration of $m_{\rm pole}$ and $\Gamma/2$ as a function of T under different fixed B. The selection of B is about 0, 15.91, 31.31, 41.57, and 51.32 M_π^2, which corresponds to 0, 0.51, 0.81, and 1 GeV^2, respectively, in our model. The inset in (b) is a zoom for the range $T \in [0.05, 0.14]$ GeV.

$\pi_{h0} = 1$. Similarly, we employ the shooting method to numerically solve the differential equations (28). Thus, the $m_{\rm pole}$ and thermal width are the real and imaginary parts of k_0, respectively.

In Fig. 8, we study the temperature dependence of $m_{\rm pole}$ and thermal widths $\Gamma/2$ of the neutral pion meson under different fixed B. From Fig. 8(a), $m_{\rm pole}$ decreases with temperature and goes to zero near $T_{\rm pc}$. On the contrary, in Fig. 8(b), for given eB, the thermal widths $(\Gamma/2)$ are small at low temperatures. Then, in the region above the critical temperature, they increase rapidly with the increase of T. Since the thermal width is related to the dissociation level, such curves naively indicate that π^0 is a well-behaved bound state at low T and becomes loose at high T. Indeed, without B, the corresponding behavior of the real and imaginary parts of the neutral pion propagator is consistent with results from LQCD simulations [85] and χPT [86], as well as holography results [71,72].

In Fig. 9, we have extracted the normalized $m_{\rm pole}$ and $\Gamma/2$ as functions of B/M_π^2 at different fixed T. Clearly, in Fig. 9(a), the normalized $m_{\rm pole}$ decreases with increasing B at finite temperatures. In vacuum, a similar behavior has already been found in lattice simulations [87] and studied by model calculations [88–90]. Meanwhile, in Fig. 9(b), we observe that when $T \lesssim T_{\rm pc}(B)$, $\Gamma/2$ exhibits strong dependence on the magnetic field and increases with B. When $T \gtrsim T_{\rm pc}(B)$, $\Gamma/2$ is slightly affected by the magnetic field, and the thermal width is almost controlled by the magnitude of the temperatures. We conclude that the magnetic field is more involved in the thermal effects below than above the critical temperature; i.e., the temperature and magnetic field are mostly entangled at moderate T. Moreover, at high temperature, $T \gg T_{\rm pc}(B)$, $\Gamma/2$ decreases with increasing B. It is interesting to note that, at high temperature, the behavior of $\Gamma/2$ is similar to $m_{{\rm scr},\parallel}$.

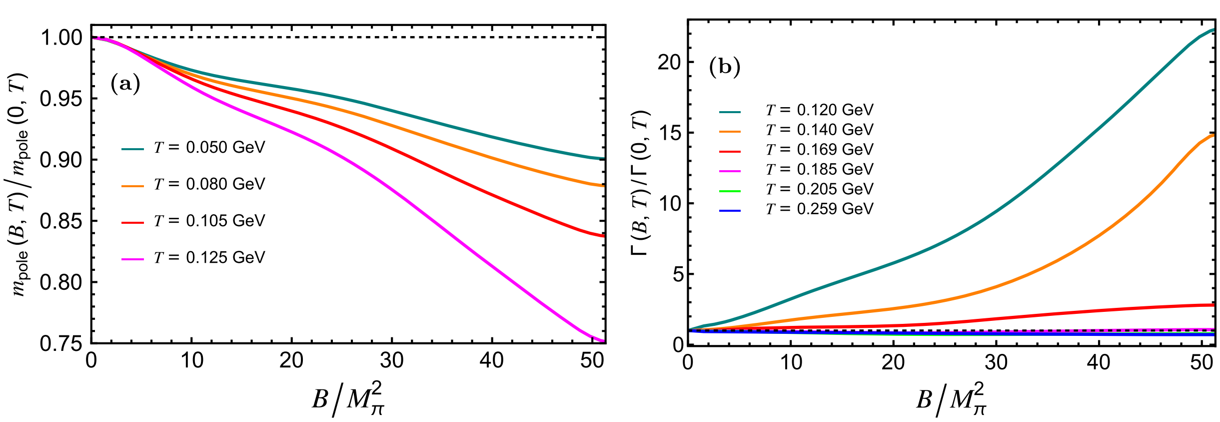

FIG. 9. Normalized $m_{\rm pole}$ and normalized $\Gamma/2$ as a function of B/M_π^2 under different fixed T, where the temperatures T are chosen as 50, 80, 105, and 125 MeV, and 120, 140, 169, 185, 205, and 299 MeV respectively.

V. CONCLUSION AND DISCUSSION

In this work, we mainly investigate the thermal properties of neutral pions within a hot and magnetized medium, including their screening masses, pole masses, and thermal widths, by using a lattice-improved soft-wall AdS/QCD model.

We introduce the magnetic field within the Einstein-Maxwell holographic model following Refs. [74,79,80]. By numerically solving the equations of motion, we obtain the full solutions with constant magnetic field. Compared with the expanding solutions in Refs. [74,79,80], the full solutions turn out to be valid in a wider range of temperature and magnetic field. Based on those numerical solutions, we consider the chiral dynamics in the soft-wall AdS/QCD model. By considering an effective coupling between the dilaton field and the flavor sector and introducing a magnetic field-dependent coupling function $g(B)$, which is fitted by the results for $T_{\rm pc}(B)$ from lattice simulations [4], we successfully capture the MC effect of chiral condensation at low temperatures and the IMC effect near the chiral transition temperature $T_{\rm pc}(B)$. It is worth mentioning that a better fitting of the chiral transition temperature $T_{\rm pc}(B)$ has been obtained, and all the other qualitative behaviors are in good agreement with the lattice simulation results [18], which shows a good description of the chiral phase transition from such an effective holographic QCD model.

Then, we study the thermal properties of the neutral pion, which is still the Goldstone boson of the chiral symmetry breaking even within a magnetic field. The temperature and magnetic field dependence of the screening masses $m_{\rm scr,\parallel}$ and $m_{\rm scr,\perp}$, characterizing the mesonic correlations in the perpendicular and vertical directions, respectively, are extracted. If one fixes the magnetic field, both $m_{\rm scr,\parallel}$ and $m_{\rm scr,\perp}$ are slightly affected by T at low temperature. In the temperature region close to transition temperatures $T_{\rm pc}(B)$, the screening masses significantly increase. Such enhanced behavior shows the connection between the screening masses and the chiral phase transition. After the phase transition, the mesons are not tightly bound, and the hot and magnetized medium starts imposing a strong impact on their properties. Then, when the temperature increases further, the two screening masses are shown to increase linearly with T and tend to be the same for different given B at extremely high temperatures. Those results are consistent with the results from effective models like NJL, confirming the effectiveness of the soft-wall holographic description on chiral dynamics.

Furthermore, we fix the temperature and study the B dependence of screening masses. Roughly speaking, the screening masses do not change much below $T_{\rm pc}$. This is reasonable since the neutral pions from our holographic model are still tightly bound states and, as neutral particles, their properties would not be changed significantly by the magnetic field. However, if we look at the results carefully, we find that at low temperature, $m_{\rm scr,\parallel}$ decreases as B grows, while $m_{\rm scr,\perp}$ increases, showing an anisotropic effect of the magnetic field at low temperature. Such a qualitative behavior can also be found from the NJL model calculation [22]. Then, when the temperature is taken to be near $T_{\rm pc}$, both $m_{\rm scr,\parallel}$ and $m_{\rm scr,\perp}$ increase with B. In the high temperature region, $m_{\rm scr,\perp}$ still increases as B grows, but $m_{\rm scr,\parallel}$ again decreases as B increases. It is worth mentioning that a similar behavior can be seen in the lattice study [23]. Moreover, we also study the ratio $u_\perp/u_\parallel$. When $T \gg T_{\rm pc}(B)$, all the curves approach 1. This indicates that the difference between $u_\perp$ and $u_\parallel$ is vanishing. The ratio $u_\perp/u_\parallel$ decreases with the increase of B. This indicates the destruction of spatial symmetry by the magnetic field. We would like to emphasize that by simply fitting the data of $T_{\rm pc}(B)$ from lattice simulations, all the qualitative behaviors for the pion properties can be consistent with lattice simulations simultaneously. In some sense, this confirms the effectiveness of the holographic QCD method.

The screening mass depicts the spatial effect, and we have seen that it can be well described by the holographic method. As for the temporal effect on the pionic sector, there are still not many data from lattice simulations. However, the extension to the holographic method is quite direct. We can obtain the poles in the complex frequency plane and get the pole mass $m_{\rm pole}$ and the thermal widths $\Gamma/2$ from their real and imaginary parts. If we fix B, we find that $m_{\rm pole}$ decreases with temperature and goes to zero near $T_{\rm pc}$, while the thermal widths $\Gamma/2$ increase monotonically with increasing T. It is interesting to see that the pole mass decreases below $T_{\rm pc}$, which is consistent with the analysis from the scaling law in the finite temperature chiral perturbation theory in [91]. In addition, it is consistent with the lattice study in [85], in which the masses of the pions are taken slightly higher than their physical values. Finally, at different fixed temperatures, $m_{\rm pole}$ monotonically decreases with B up to $1~\mathrm{GeV}^2$. This behavior is qualitatively consistent with the lattice-improved NJL study in [22] while it differs from the NJL calculation in Ref. [35], in which $m_{\rm pole}$ decreases when $B < 0.8~\mathrm{GeV}^2$ and increases when $B > 0.8~\mathrm{GeV}^2$. Being similar to the behavior of $m_{\rm scr,\parallel}$, we can also see that the thermal widths of the π^0 slightly decrease as B grows above the critical temperature. In this work, we find that the thermal properties of magnetized pions are mainly determined by the temperature itself at high T. These are preliminary results of the dependence on the magnetic field since such a weak dependence would be easily washed out by other effects, for example, the backaction from the metric, and a full calculation will be required in future work.

In the present study, we see that by fitting our holographic model using the condensation data from the lattice, the model can capture most of the qualitative behaviors, especially for the thermal properties of pions. Because of the limitation from our current numerical techniques, we cannot compare the zero temperature behavior of the pole masses under the magnetic field or check the main difference between our results and the NJL studies in Ref. [35]. We will leave this to future work. Furthermore, the recent LQCD simulation results indicate that within the B range of approximately 4 to 9 GeV^2, chiral condensation switches from a crossover to first order at a critical endpoint located in this range [92]. It is also interesting to extend our study to the stronger magnetic field case.

ACKNOWLEDGMENTS

N. W. thanks Wei-Jiang Liang for valuable discussions. This work is supported by the National Natural Science Foundation of China (NSFC) under Grants No. 12275108 and No. 12305142, the Science and Technology Planning Project of Guangzhou, China under Grant No. 2024A04J3243, and the Fundamental Research Funds for the Central Universities under Grant No. 21622324. J. C. is supported by the National Natural Science Foundation of China (NSFC) under Grant No. 12365020.

[1] V. Skokov, A. Y. Illarionov, and V. Toneev, Estimate of the magnetic field strength in heavy-ion collisions, Int. J. Mod. Phys. A **24**, 5925 (2009).

[2] W.-T. Deng and X.-G. Huang, Event-by-event generation of electromagnetic fields in heavy-ion collisions, Phys. Rev. C **85**, 044907 (2012).

[3] V. Voronyuk, V. D. Toneev, W. Cassing, E. L. Bratkovskaya, V. P. Konchakovski, and S. A. Voloshin, (Electro-)magnetic field evolution in relativistic heavy-ion collisions, Phys. Rev. C **83**, 054911 (2011).

[4] G. S. Bali, F. Bruckmann, G. Endrodi, Z. Fodor, S. D. Katz, S. Krieg, A. Schafer, and K. K. Szabo, The QCD phase diagram for external magnetic fields, J. High Energy Phys. 02 (2012) 044.

[5] J. O. Andersen, W. R. Naylor, and A. Tranberg, Phase diagram of QCD in a magnetic field: A review, Rev. Mod. Phys. **88**, 025001 (2016).

[6] V. A. Miransky and I. A. Shovkovy, Quantum field theory in a magnetic field: From quantum chromodynamics to graphene and Dirac semimetals, Phys. Rep. **576**, 1 (2015).

[7] K. Fukushima, D. E. Kharzeev, and H. J. Warringa, The chiral magnetic effect, Phys. Rev. D **78**, 074033 (2008).

[8] D. E. Kharzeev, The chiral magnetic effect and anomaly-induced transport, Prog. Part. Nucl. Phys. **75**, 133 (2014).

[9] D. E. Kharzeev, L. D. McLerran, and H. J. Warringa, The effects of topological charge change in heavy ion collisions: “Event by event P and CP violation”, Nucl. Phys. **A803**, 227 (2008).

[10] D. E. Kharzeev and D. T. Son, Testing the chiral magnetic and chiral vortical effects in heavy ion collisions, Phys. Rev. Lett. **106**, 062301 (2011).

[11] M. N. Chernodub, Superconductivity of QCD vacuum in strong magnetic field, Phys. Rev. D **82**, 085011 (2010).

[12] M. N. Chernodub, Spontaneous electromagnetic superconductivity of vacuum in strong magnetic field: Evidence from the Nambu–Jona-Lasinio model, Phys. Rev. Lett. **106**, 142003 (2011).

[13] G. Cao and X.-G. Huang, Electromagnetic triangle anomaly and neutral pion condensation in QCD vacuum, Phys. Lett. B **757**, 1 (2016).

[14] G. S. Bali, F. Bruckmann, G. Endrödi, S. D. Katz, and A. Schäfer, The QCD equation of state in background magnetic fields, J. High Energy Phys. 08 (2014) 177.

[15] V. P. Gusynin, V. A. Miransky, and I. A. Shovkovy, Dimensional reduction and catalysis of dynamical symmetry breaking by a magnetic field, Nucl. Phys. **B462**, 249 (1996).

[16] P. V. Buividovich, M. N. Chernodub, E. V. Luschevskaya, and M. I. Polikarpov, Numerical study of chiral symmetry breaking in non-Abelian gauge theory with background magnetic field, Phys. Lett. B **682**, 484 (2010).

[17] V. V. Braguta, P. V. Buividovich, T. Kalaydzhyan, S. V. Kuznetsov, and M. I. Polikarpov, The chiral magnetic effect and chiral symmetry breaking in SU(3) quenched lattice gauge theory, Phys. At. Nucl. **75**, 488 (2012).

[18] G. S. Bali, F. Bruckmann, G. Endrodi, Z. Fodor, S. D. Katz, and A. Schafer, QCD quark condensate in external magnetic fields, Phys. Rev. D **86**, 071502 (2012).

[19] J. O. Andersen, QCD phase diagram in a constant magnetic background: Inverse magnetic catalysis: Where models meet the lattice, Eur. Phys. J. A **57**, 189 (2021).

[20] R. Alkofer, P. A. Amundsen, and K. Langfeld, Chiral symmetry breaking and pion properties at finite temperatures, Z. Phys. C **42**, 199 (1989).

[21] B. Sheng, Y. Wang, X. Wang, and L. Yu, Pole and screening masses of neutral pions in a hot and magnetized medium: A comprehensive study in the Nambu–Jona-Lasinio model, Phys. Rev. D **103**, 094001 (2021).

[22] B.-k. Sheng, X. Wang, and L. Yu, Impacts of inverse magnetic catalysis on screening masses of neutral pions and sigma mesons in hot and magnetized quark matter, Phys. Rev. D **105**, 034003 (2022).

[23] H. T. Ding, S. T. Li, J. H. Liu, and X. D. Wang, Chiral condensates and screening masses of neutral pseudoscalar mesons in thermomagnetic QCD medium, Phys. Rev. D **105**, 034514 (2022).

[24] R. Wen, S. Yin, W.-j. Fu, and M. Huang, Functional renormalization group study of neutral and charged pions in magnetic fields in the quark-meson model, Phys. Rev. D **108**, 076020 (2023).

[25] H.-T. Ding, S.-T. Li, S. Mukherjee, A. Tomiya, and X.-D. Wang, Meson masses in external magnetic fields with HISQ

fermions, Proc. Sci., LATTICE2019 (**2020**) 250 [arXiv:2001.05322].
[26] G. S. Bali, B. B. Brandt, G. Endrődi, and B. Gläßle, Meson masses in electromagnetic fields with Wilson fermions, Phys. Rev. D **97**, 034505 (2018).
[27] G. S. Bali, B. B. Brandt, G. Endrődi, and B. Gläße, Pion decay in magnetic fields, EPJ Web Conf. **175**, 13005 (2018).
[28] R. Bignell, W. Kamleh, and D. Leinweber, Pion magnetic polarisability using the background field method, Phys. Lett. B **811**, 135853 (2020).
[29] E. V. Luschevskaya, O. E. Solovjeva, and O. V. Teryaev, Determination of the properties of vector mesons in external magnetic field by quenched SU(3) lattice QCD, J. High Energy Phys. 09 (2017) 142.
[30] J. O. Andersen, Chiral perturbation theory in a magnetic background—finite-temperature effects, J. High Energy Phys. 10 (2012) 005.
[31] M. M. Aung, S. Leupold, E. Perotti, and Y. Yan, Electromagnetic form factors of the transition from the Delta to the nucleon, arXiv:2401.17756.
[32] F. Alvarado, D. An, L. Alvarez-Ruso, and S. Leupold, Light quark mass dependence of nucleon electromagnetic form factors in dispersively modified chiral perturbation theory, Phys. Rev. D **108**, 114021 (2023).
[33] Z. Wang and P. Zhuang, Meson properties in magnetized quark matter, Phys. Rev. D **97**, 034026 (2018).
[34] S. Fayazbakhsh and N. Sadooghi, Weak decay constant of neutral pions in a hot and magnetized quark matter, Phys. Rev. D **88**, 065030 (2013).
[35] J. Li, G. Cao, and L. He, Gauge independence of pion masses in a magnetic field within the Nambu–Jona-Lasinio model, Phys. Rev. D **104**, 074026 (2021).
[36] K. Kamikado and T. Kanazawa, Chiral dynamics in a magnetic field from the functional renormalization group, J. High Energy Phys. 03 (2014) 009.
[37] J. M. Pawlowski and M. Reichert, Quantum gravity from dynamical metric fluctuations, arXiv:2309.10785.
[38] J. M. Maldacena, The large N limit of superconformal field theories and supergravity, AIP Conf. Proc. **484**, 51 (1999).
[39] S. S. Gubser, I. R. Klebanov, and A. M. Polyakov, Gauge theory correlators from noncritical string theory, Phys. Lett. B **428**, 105 (1998).
[40] E. Witten, Anti-de Sitter space and holography, Adv. Theor. Math. Phys. **2**, 253 (1998).
[41] J. Erlich, E. Katz, D. T. Son, and M. A. Stephanov, QCD and a holographic model of hadrons, Phys. Rev. Lett. **95**, 261602 (2005).
[42] A. Karch, E. Katz, D. T. Son, and M. A. Stephanov, Linear confinement and AdS/QCD, Phys. Rev. D **74**, 015005 (2006).
[43] S. S. Gubser and A. Nellore, Mimicking the QCD equation of state with a dual black hole, Phys. Rev. D **78**, 086007 (2008).
[44] S. S. Gubser, A. Nellore, S. S. Pufu, and F. D. Rocha, Thermodynamics and bulk viscosity of approximate black hole duals to finite temperature quantum chromodynamics, Phys. Rev. Lett. **101**, 131601 (2008).
[45] U. Gursoy and E. Kiritsis, Exploring improved holographic theories for QCD: Part I, J. High Energy Phys. 02 (2008) 032.
[46] U. Gursoy, E. Kiritsis, and F. Nitti, Exploring improved holographic theories for QCD: Part II, J. High Energy Phys. 02 (2008) 019.
[47] S. J. Brodsky, G. F. de Teramond, H. G. Dosch, and J. Erlich, Light-front holographic QCD and emerging confinement, Phys. Rep. **584**, 1 (2015).
[48] P. Colangelo, F. De Fazio, F. Giannuzzi, F. Jugeau, and S. Nicotri, Light scalar mesons in the soft-wall model of AdS/QCD, Phys. Rev. D **78**, 055009 (2008).
[49] T. Gherghetta, J. I. Kapusta, and T. M. Kelley, Chiral symmetry breaking in the soft-wall AdS/QCD model, Phys. Rev. D **79**, 076003 (2009).
[50] T. M. Kelley, S. P. Bartz, and J. I. Kapusta, Pseudoscalar mass spectrum in a soft-wall model of AdS/QCD, Phys. Rev. D **83**, 016002 (2011).
[51] D. Li, M. Huang, and Q.-S. Yan, A dynamical soft-wall holographic QCD model for chiral symmetry breaking and linear confinement, Eur. Phys. J. C **73**, 2615 (2013).
[52] D. Li and M. Huang, Dynamical holographic QCD model for glueball and light meson spectra, J. High Energy Phys. 11 (2013) 088.
[53] Y.-Q. Sui, Y.-L. Wu, Z.-F. Xie, and Y.-B. Yang, Prediction for the mass spectra of resonance mesons in the soft-wall AdS/QCD with a modified 5D metric, Phys. Rev. D **81**, 014024 (2010).
[54] A. Ballon-Bayona and L. A. H. Mamani, Nonlinear realization of chiral symmetry breaking in holographic soft wall models, Phys. Rev. D **102**, 026013 (2020).
[55] E. Folco Capossoli, M. A. Martín Contreras, D. Li, A. Vega, and H. Boschi-Filho, Hadronic spectra from deformed AdS backgrounds, Chin. Phys. C **44**, 064104 (2020).
[56] Y. Chen and M. Huang, Holographic QCD model for $N_f = 4$, Phys. Rev. D **105**, 026021 (2022).
[57] H. A. Ahmed, Y. Chen, and M. Huang, $D_{(s)}$-mesons semileptonic form factors in four-flavor holographic QCD, Phys. Rev. D **109**, 026008 (2024).
[58] X. Guo, J.-J. Jiang, X. Liu, X. Chen, D. Xiang, and X.-H. Li, Doubly-heavy tetraquark at finite temperature in a holographic model, Eur. Phys. J. C **84**, 101 (2024).
[59] K. Chelabi, Z. Fang, M. Huang, D. Li, and Y.-L. Wu, Chiral phase transition in the soft-wall model of AdS/QCD, J. High Energy Phys. 04 (2016) 036.
[60] K. Chelabi, Z. Fang, M. Huang, D. Li, and Y.-L. Wu, Realization of chiral symmetry breaking and restoration in holographic QCD, Phys. Rev. D **93**, 101901 (2016).
[61] D. Li and M. Huang, Chiral phase transition of QCD with $N_f = 2 + 1$ flavors from holography, J. High Energy Phys. 02 (2017) 042.
[62] J. Chen, S. He, M. Huang, and D. Li, Critical exponents of finite temperature chiral phase transition in soft-wall AdS/QCD models, J. High Energy Phys. 01 (2019) 165.
[63] F. R. Brown, F. P. Butler, H. Chen, N. H. Christ, Z.-h. Dong, W. Schaffer, L. I. Unger, and A. Vaccarino, On the existence of a phase transition for QCD with three light quarks, Phys. Rev. Lett. **65**, 2491 (1990).
[64] H.-T. Ding, F. Karsch, and S. Mukherjee, Thermodynamics of strong-interaction matter from lattice QCD, Int. J. Mod. Phys. E **24**, 1530007 (2015).
[65] M. Lv, D. Li, and S. He, Pion condensation in a soft-wall AdS/QCD model, J. High Energy Phys. 11 (2019) 026.

[66] X. Cao, H. Liu, D. Li, and G. Ou, QCD phase diagram at finite isospin chemical potential and temperature in an IR-improved soft-wall AdS/QCD model, Chin. Phys. C **44**, 083106 (2020).

[67] X. Chen, D. Li, D. Hou, and M. Huang, Quarkyonic phase from quenched dynamical holographic QCD model, J. High Energy Phys. 03 (2020) 073.

[68] Y. Chen, D. Li, and M. Huang, Inhomogeneous chiral condensation under rotation in the holographic QCD, Phys. Rev. D **106**, 106002 (2022).

[69] X. Cao, J. Chao, H. Liu, and D. Li, Thermalization and prethermalization in the soft-wall AdS/QCD model, Phys. Rev. D **107**, 086001 (2023).

[70] X. Cao, M. Baggioli, H. Liu, and D. Li, Pion dynamics in a soft-wall AdS-QCD model, J. High Energy Phys. 12 (2022) 113.

[71] X. Cao, S. Qiu, H. Liu, and D. Li, Thermal properties of light mesons from holography, J. High Energy Phys. 08 (2021) 005.

[72] X. Cao, H. Liu, and D. Li, Pion quasiparticles and QCD phase transitions at finite temperature and isospin density from holography, Phys. Rev. D **102**, 126014 (2020).

[73] W. Liang, X. Cao, H. Liu, and D. Li, Pion quasiparticles in isospin medium from holography, Phys. Rev. D **108**, 096019 (2023).

[74] D. Li, M. Huang, Y. Yang, and P.-H. Yuan, Inverse magnetic catalysis in the soft-wall model of AdS/QCD, J. High Energy Phys. 02 (2017) 030.

[75] D. M. Rodrigues, D. Li, E. Folco Capossoli, and H. Boschi-Filho, Chiral symmetry breaking and restoration in $2+1$ dimensions from holography: Magnetic and inverse magnetic catalysis, Phys. Rev. D **98**, 106007 (2018).

[76] D. M. Rodrigues, D. Li, E. Folco Capossoli, and H. Boschi-Filho, Finite density effects on chiral symmetry breaking in a magnetic field in $2+1$ dimensions from holography, Phys. Rev. D **103**, 066022 (2021).

[77] Z. Fang, Anomalous dimension, chiral phase transition and inverse magnetic catalysis in soft-wall AdS/QCD, Phys. Lett. B **758**, 1 (2016).

[78] J. P. Boyd, *Chebyshev and Fourier Spectral Methods* (Dover Publications, Mineola, NY, 2001).

[79] K. A. Mamo, Inverse magnetic catalysis in holographic models of QCD, J. High Energy Phys. 05 (2015) 121.

[80] D. Dudal, D. R. Granado, and T. G. Mertens, No inverse magnetic catalysis in the QCD hard and soft wall models, Phys. Rev. D **93**, 125004 (2016).

[81] K. A. Olive *et al.* (Particle Data Group), Review of particle physics, Chin. Phys. C **38**, 090001 (2014).

[82] A. Cherman, T. D. Cohen, and E. S. Werbos, The chiral condensate in holographic models of QCD, Phys. Rev. C **79**, 045203 (2009).

[83] A. S. Miranda, C. A. Ballon Bayona, H. Boschi-Filho, and N. R. F. Braga, Black-hole quasinormal modes and scalar glueballs in a finite-temperature AdS/QCD model, J. High Energy Phys. 11 (2009) 119.

[84] D. T. Son and A. O. Starinets, Minkowski space correlators in AdS/CFT correspondence: Recipe and applications, J. High Energy Phys. 09 (2002) 042.

[85] B. B. Brandt, A. Francis, H. B. Meyer, and D. Robaina, Pion quasiparticle in the low-temperature phase of QCD, Phys. Rev. D **92**, 094510 (2015).

[86] D. T. Son and M. A. Stephanov, Real time pion propagation in finite temperature QCD, Phys. Rev. D **66**, 076011 (2002).

[87] H. T. Ding, S. T. Li, A. Tomiya, X. D. Wang, and Y. Zhang, Chiral properties of $(2+1)$-flavor QCD in strong magnetic fields at zero temperature, Phys. Rev. D **104**, 014505 (2021).

[88] Z. Xing, J. Chao, L. Chang, and Y.-x. Liu, Exposing the effect of the p-wave component in the pion triplet under a strong magnetic field, Phys. Rev. D **105**, 114003 (2022).

[89] F. Lin, K. Xu, and M. Huang, Magnetism of QCD matter and the pion mass from tensor-type spin polarization and the anomalous magnetic moment of quarks, Phys. Rev. D **106**, 016005 (2022).

[90] J. Chao and Y.-X. Liu, Dimensional reduction and the generalized pion in a magnetic field within the NJL model, Phys. Rev. D **107**, 074038 (2023).

[91] D. T. Son and M. A. Stephanov, Pion propagation near the QCD chiral phase transition, Phys. Rev. Lett. **88**, 202302 (2002).

[92] M. D'Elia, L. Maio, F. Sanfilippo, and A. Stanzione, Phase diagram of QCD in a magnetic background, Phys. Rev. D **105**, 034511 (2022).